

Forces, moment, and wave pattern for surface combatant in regular head waves

Part I. Measurement systems and uncertainty assessment

L. Gui, J. Longo, B. Metcalf, J. Shao, F. Stern

674

Abstract A model-scale naval surface combatant, DTMB 5512, is studied experimentally in steady forward speed and regular head waves with the Iowa Institute of Hydraulic Research towing-tank facilities. Unsteady resistance, heave force, pitch moment and free-surface elevations are investigated with different measurement systems for a fairly wide range of test conditions. Test data is procured for validation of RANS computational fluid dynamics codes and for understanding the physics of unsteady ship hydrodynamics. In the first part of the two-part paper, details of data reductions, measurement systems and uncertainty assessment procedures are provided.

1 Introduction

Rapid advancements in computational fluid dynamics (CFD) have enabled the solution of increasingly complex ship hydrodynamics simulations (Arabshahi et al. 1998, Wilson et al. 1998, Landrini et al. 1999, Alessandrini and Delhommeau 1999). For development and validation of CFD codes, much more detailed model-scale, surface ship experimental data is required (Stern et al. 1998, ITTC 1999). To keep pace with the CFD simulations, the experimental fluid dynamics (EFD) community is expected to design and execute experiments that consider more real-world flow conditions and address a variety of physics of interest with advanced measurement techniques.

The goal of the present work is to support the CFD code development for unsteady ship hydrodynamics through towing-tank experiments for forward-speed diffraction problem, i.e., ship model advancing in regular head waves, but restrained from motions. Currently, the forward-speed diffraction problem plays an important role in engineering approaches, which use linear, potential flow, strip theory

for ship and platform motions, and the exciting forces for motions are a solution of the forward-speed diffraction problem. This model problem can be considered a first step in the merging of separate fields of resistance and propulsion, seakeeping, and maneuvering. The specific physical problem of interest is a 1:46.6 scale model of a modern surface combatant, DTMB 5512, advancing in regular head waves. The experiments include the measurement of unsteady resistance, heave force, and pitch moment for a wide range of incident waves for identification of the effects of the Froude number, wavelength and wave steepness. In addition, a detailed mapping of unsteady free-surface elevations is conducted for a selected test condition.

Related studies include those of Journee (1992) and Rhee and Stern (1998) who conducted, respectively, experimental investigations and CFD simulations of unsteady forces and moment for Wigley hullforms. For measuring the unsteady free-surface elevations around a ship model, Ohkusu (1990) described two methods, i.e., with wave probes installed on the towing carriage for acquiring data point by point and with wave probes fixed in the towing tank for line-by-line measurements. Kanai (1985) described a grid projection method for a whole-field measurement of the instantaneous wave field. Another optical method was used by Nishio et al. (1998) for mapping the wave height distributions around a ship hull in regular waves. In comparison to previous works, the present study provides much more detailed data with rigorous uncertainty assessment for CFD validation and systematic analyses of the flow physics in ship hydrodynamics covering linear and non-linear responses of forces and moment, unsteady free-surface elevations, and free-surface turbulence. In the following, details of data reductions, measurement systems, and uncertainty assessments are described.

Received: 4 October 2000 / Accepted: 23 April 2001

L. Gui (✉), J. Longo, B. Metcalf, J. Shao, F. Stern
Iowa Institute of Hydraulic Research (IIHR)
The University of Iowa
Iowa City, IA 52242, USA
e-mail: guil@purdue.edu

This research was sponsored by Office of Naval Research under Grant N00014-96-1-0018 under the administration of Dr. E.P. Rood. The generous loan of the servo-type and acoustic wave probes by Prof. Yasuyuki Toda, Department of Global Engineering, University of Osaka, Osaka, Japan is gratefully acknowledged.

2 Measurement systems

2.1 Data reduction

The tests are conducted in the IIHR towing tank. A plunger-type wave-maker is utilized for generation of regular head waves (Longo et al. 1998). An automated, moveable sidewall wave-damper system is used for wave absorption. DTMB model 5512 is selected for the tests. Two right-handed Cartesian coordinate systems are used in the towing tank: A relative coordinate system (x, y, z) is attached to the moving test model with the origin at the

intersection of the undisturbed free surface and forward perpendicular (FP) of the model, and an absolute coordinate system (X, Y, Z) is fixed in the towing tank. The axes of the coordinate systems are normalized with model length and directed downstream, transverse, and upward, respectively. The unsteady test conditions are determined with Froude number (Fr), wavelength (λ) and wave steepnesses (Ak). Fr and Ak are defined as

$$Fr = U_c / \sqrt{gL} \quad (1)$$

$$Ak = 2\pi A / \lambda \quad (2)$$

where g is the local gravity acceleration, and L is the model length. When the test condition (i.e. Fr , λ and Ak) is selected, the carriage speed U_c is determined with Fr (Eq. 1), the incident wave amplitude A is determined with Ak and λ (Eq. 2). The frequency of the regular head wave f_w and the frequency of the encounter wave f_e are determined as

$$f_w = \sqrt{g / (2\pi\lambda)} \quad (3)$$

$$f_e = f_w + U_c / \lambda \quad (4)$$

In the present study, forces and moment data are procured for a fairly wide range of conditions, i.e., $Fr = 0.19 \sim 0.41$, $Ak = 0.025 \sim 0.075$, and $\lambda = 1.524 \sim 4.572$ m. The free-surface elevation measurements are conducted in the area of $-0.25 \leq x \leq 1.35$, $0 \leq y \leq 0.4$. This area is divided into two regions: (1) The farfield region beyond the maximum beam of the model ($0.08 \leq y \leq 0.4$) and (2) the nearfield region at the bow and stern ($0 \leq y \leq 0.08$). In the farfield region, a longitudinal cut method is employed to determine unsteady free-surface elevations at thousands of points on a constant y -cut in roughly 20 carriage runs. In the nearfield region, the free-surface elevations are measured point by point with wave probes attached to the moving carriage to obtain detailed information including the free-surface turbulence and high-frequency responses.

The variables of interest are the resistant coefficient (C_T), heave force coefficient (C_H), pitch moment coefficient (C_M), and non-dimensional free-surface elevations (ζ_T), which are defined as

$$C_T(t) = F_x(t) / (0.5\rho U_c^2 S) \quad (5)$$

$$C_H(t) = F_z(t) / (0.5\rho U_c^2 S) \quad (6)$$

$$C_M(t) = M_y(t) / (0.5\rho U_c^2 SL) \quad (7)$$

$$\zeta_T(x, y, t) = z(x, y, t) / L \quad (8)$$

where F_x , F_z , M_y , and z are the measured time-varying resistance, heave force, pitch moment, and free-surface elevation, respectively; ρ is the towing-tank water density; and S is the design-offsets wetted surface area for the static condition.

Since the data acquisition is not synchronized with the wave-maker, a time (or phase) reference is needed with the acquired time histories, i.e., the incident wave at $x = 0$, i.e.,

$$\zeta_1(t) = \frac{A}{L} \cos(2\pi f_e t + \gamma_I) \quad (9)$$

The amplitude and frequency of the reference wave are known, but the initial phase γ_I is determined through

analysis of the incident-wave time history. In the tests, the incident-wave records are measured upstream ($x \neq 0$) of the model, in regions where the waveform is unaffected by the model, with a tank-fixed wave probe (forces and moment, farfield elevations) or a trailer-mounted wave probe (nearfield elevations). Thus, a phase shift is necessary to determine the reference phase.

Unsteady time histories are reconstructed with Fourier series (FS). When the phase of the reference wave, i.e., the incident wave at $x = 0$, is set to zero, the FS for time history X ($X = C_T, C_H, C_M, \zeta_T$) is determined as follows:

$$X_F(t) = \frac{X_0}{2} + \sum_{n=1}^N X_n \cos(2\pi n f_e t + \Delta\gamma_n) \quad (10)$$

$$\Delta\gamma_n = \gamma_n - \gamma_I \quad (11)$$

$$X_n = \sqrt{a_n^2 + b_n^2} \quad (12)$$

$$\gamma_n = \tan^{-1}(b_n / a_n) \quad (13)$$

$$a_n = \frac{2}{T} \int_0^{T'} X(t) \cos(2\pi n f_e t) dt \quad \text{for } n = 0, 1, 2, 3, \dots \quad (14)$$

$$b_n = -\frac{2}{T} \int_0^{T'} X(t) \sin(2\pi n f_e t) dt \quad \text{for } n = 1, 2, 3, \dots \quad (15)$$

wherein X_F is the reconstructed time history; X_n is the n th-order harmonic amplitude; γ_n is the corresponding phase; N is the order of the FS and chosen high enough to include all important frequency components. $\Delta\gamma_n$ is the harmonic phase adjusted with the reference wave, and for forces and moment, it is the phase lead relative to the reference wave. Time interval T is a multiple of the encounter wave period $T (=1/f_e)$.

2.2

Measurement system for forces and moment

The measurement system for the forces and moment consists of a four-channel (two force, two moment) strain-gage loadcell and signal conditioner and a carriage-based PC with 12-bit AD card. A shore-based capacitance-wire probe and PC are used to sample the incident wave for determining the reference phase γ_I . A pair of photoelectric switches is used to synchronize data acquisition start times for the carriage-based and shore-based measurement systems. The load cell is mounted at the mid-ship of the model ($x = 0, y = 0.5$) and the towing height is $z = 0.0641$. A sketch of the measurement system is given in Fig. 1.

The signals are sampled from the loadcell and the wave probe, amplified and filtered in the signal conditioners, digitized through AD conversion in the carriage and shore-based PCs, and finally converted to time histories of forces and moment ($C_T(t), C_H(t), C_M(t)$) and incident wave ($\zeta_1(t)$). Each time history consists of 2048 samples producing acquisition times of 30, 10, 15, and 10 s for $Fr = 0.19, 0.28, 0.34$, and 0.41 , respectively. The phase of

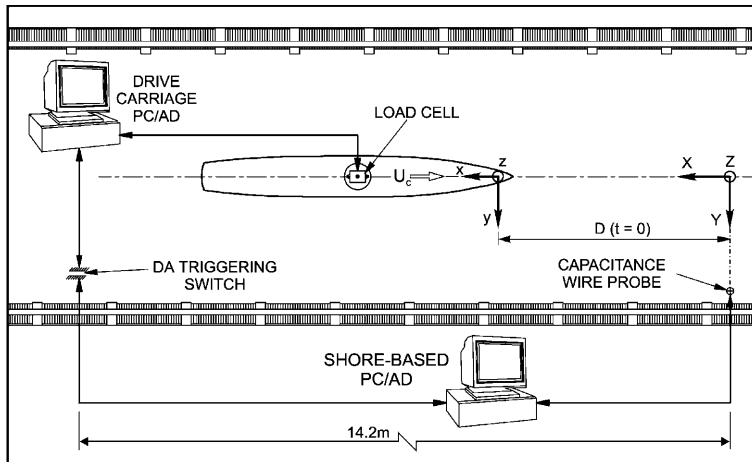


Fig. 1. Experimental setup for forces and moment

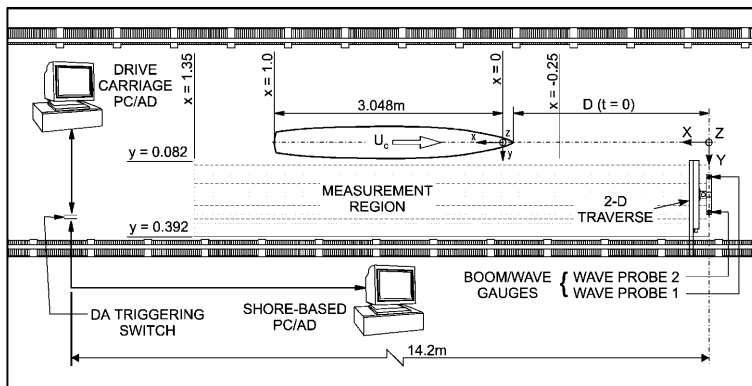


Fig. 2. Experimental setup for farfield free surface

the incident wave at the position of the capacitance-wire probe is determined with the first-order FS harmonic phase of time history $z_I(t)$, i.e., $\gamma_{z,1}$. When the data acquisition is started ($t = 0$), the wave probe is in advance of the FP of the model by a distance $D (=11.99 \text{ m})$. Therefore, a delay of $2\pi D/\lambda$ is required to determine the reference phase:

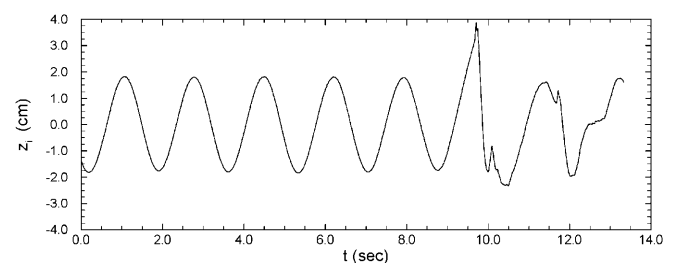
$$\gamma_I = \gamma_{z,1} - 2\pi \frac{D}{\lambda} \quad (16)$$

2.3 Farfield free surface elevations

A longitudinal wave cut method with two wave probes is used to measure the unsteady farfield free-surface elevations. As shown in Fig. 2, the measurement system consists of a sidewall-mounted boom, servo-type wave probe (probe 1) and signal conditioner, acoustic-type wave probe (probe 2) and signal conditioner, 2D automated traverse system, shore-based PC with 12-bit AD card, carriage-based PC with 12-bit AD card, and a pair of photoelectric switches for external data acquisition triggering. The measurement is completed with 32 longitudinal (constant- y) cuts, spaced at $\Delta y = 0.01$ between the maximum beam of the model and the sidewall damper. The data acquisition is triggered with photoelectric switches 9 s prior to the model FP passing the wave probes and ended when the measurement region is completely scanned. The total time interval for data acquisition is

13.3 s and 2700 samples are recorded in every carriage run. A total of 15–25 carriage runs are performed at each constant- y cut to ensure a satisfactory distribution of incident-wave phases at the beginning of the raw time histories. One of the raw time histories ($z_i(y, t)$) taken at $y = 0.082$ is shown in Fig. 3. Note that the incident wave is recorded in the initial 9 s and this information is used to determine the initial phase (γ_i).

In the model coordinate system (x, y, z), the data acquisition at each y -cut is started at $x = -D/L$ and the wave probe moves in the positive x -direction with constant carriage speed U_c . As such, the x -position of the measurement is dependent on the sample time (t). Therefore, the measured raw time histories are converted to spatial distributions of the free-surface elevations as

Fig. 3. Sample time history of farfield free-surface elevation at $y = 0.082$

$$\zeta_i(x, y) = \frac{z_i(y, t)}{L} \quad \text{with } x = \frac{U_c t - D}{L} \quad (17)$$

Figure 4 shows the spatial distributions of free-surface elevation obtained in 14 runs at $y = 0.082$. Based on a group of spatial distributions of the unsteady free-surface elevations at a certain y -cut, a distribution of free-surface elevation on the initial phase is obtained for every x -position. As an example, symbols in Fig. 5 show the distribution of free-surface elevation on the initial phase at $x = 0.169$ in the cut of $y = 0.082$. After the dispersed distribution is fitted with a continuous polynomial curve, see the curve in Fig. 5, FS coefficients are determined with

$$a_n = \frac{1}{\pi} \int_{-\pi}^{\pi} \zeta_p(\gamma) \cos(n\gamma) d\gamma \quad (18)$$

$$b_n = -\frac{1}{\pi} \int_{-\pi}^{\pi} \zeta_p(\gamma) \sin(n\gamma) d\gamma \quad (19)$$

wherein $\zeta_p(\gamma)$ is the polynomial fit of the dispersed distribution of ($\zeta_{is}\gamma_i$), and it depends on position (x, y).

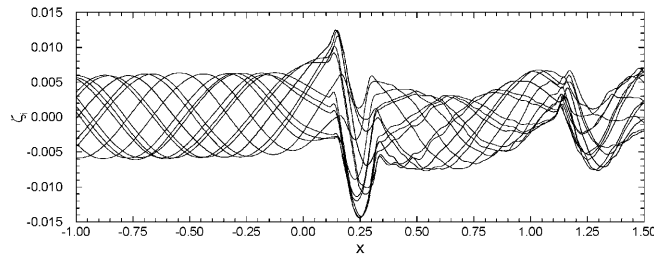


Fig. 4. Spatial distributions of farfield free-surface elevations at $y = 0.008$

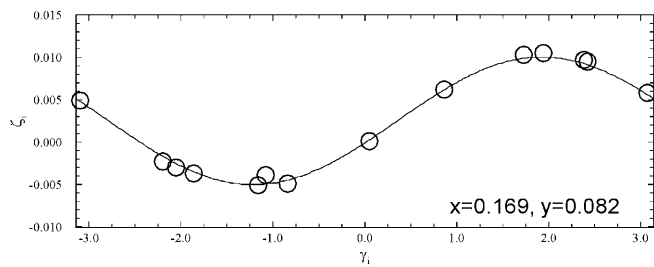


Fig. 5. Distribution of the free-surface elevation on the initial phase at one point of a y -cut

According to Eqs. 12, 13, 18 and 19, the FS harmonic amplitude and phase can be computed. For each y -cut, the first point x_0 ($x_0 = -D/L$, $D = 14.45$ m) is upstream and far from the model. Therefore, the first-order FS harmonic phase (γ_0) at x_0 represents the phase of the local incident wave. A phase delay of $2\pi D/\lambda$ is considered for the incident wave at $x = 0$. In addition, because the data is obtained at different times for different x -positions in each y -cut, a time shift of $\Delta t = (x-x_0)L/U_c$ should be taken into account, and the corresponding phase shift is $2\pi f_e \Delta t$. Finally, the reference phase is determined with

$$\gamma_I = \gamma_0 - 2\pi \frac{D}{\lambda} + 2\pi f_e \frac{D + xL}{U_c} \quad (20)$$

Note that Eq. 20 is valid only for constant y .

2.4

Nearfield free-surface elevations

The nearfield measurement system consists of the same equipment as for the farfield measurement system, but is arranged differently. The two wave probes are attached to the moving carriage. As shown in Fig. 6, probe 2 is installed forward of the model on the trailer for acquiring the incident wave and probe 1 is installed on a trailer-mounted automated traverse for measuring the unsteady free-surface elevations. The measurement area is mapped with 22 and 26 variably-spaced (in the x -coordinate) transverse cuts at the bow and stern, respectively. The measurement location spacing in the y -coordinate is variable, but mostly $\Delta y = 0.005$. Two points are measured in each carriage run with a probe movement. At each measurement point, 3000 samples are acquired in a 9-s time interval. In the data acquisition procedure, time histories for the unsteady free-surface ($z(x, y, t)$) and incident wave ($z_I(t)$) are obtained. In the post-processing procedure, the reference phase is determined according to the time history of the incident wave and the FS harmonic amplitudes and phases are computed for unsteady free-surface elevations. The phase of the incident wave at probe 2 is determined with the first harmonic phase of the sampled wave elevation $\gamma_{z,1}$. Since wave probe 2 is installed at $x = -D/L$ ($D=1.905$ m), a phase delay of $2\pi D/\lambda$ is considered to determine the reference phase:

$$\gamma_I = \gamma_{z,1} - 2\pi \frac{D}{\lambda} \quad (21)$$

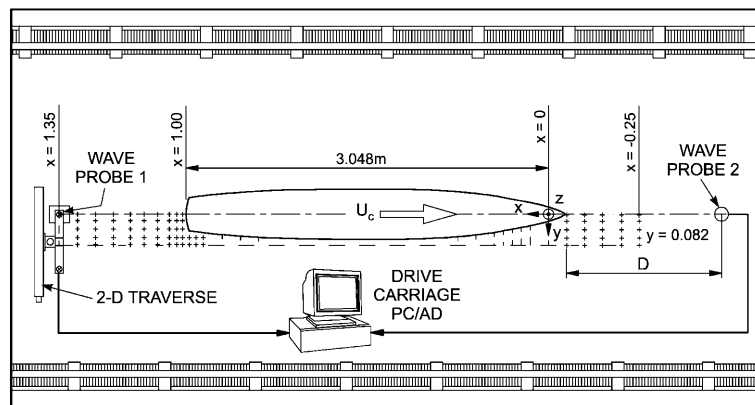


Fig. 6. Experimental setup for nearfield free surface

3

Uncertainty assessment

Uncertainty assessments are completed for the results on three levels: raw time histories, FS harmonics, and the FS-reconstructed time histories. Following the AIAA standard (S-017A-1999), the uncertainty of a measurement variable is defined as the root sum square (RSS) of the bias limit and precision limit for a 95% confidence level. For a raw time history, the bias limit is estimated according to data reduction equations and elementary bias limits, and the precision limit is estimated with repeated end-to-end data-acquisition and reduction cycles. However, the estimation procedures of the bias and precision limits for the FS harmonics and the precision limits for the reconstructed time histories are not described in detail in the standard. In the following, the uncertainty assessment procedures for FS harmonics and FS-reconstructed time histories will be discussed and a summary of uncertainty assessment results for current measurements will be provided.

3.1

FS harmonics

In order to determine the bias limits for the FS harmonic amplitudes and phases, it is assumed that the measured value X deviates from the real value X' with a bias error β . When the random error is not considered, the real and measured value are related with

$$X = X' + \beta \quad (22)$$

The bias error β is not a constant, and it is usually a function of the measurement value. For simplification, we assume the relation is linear, i.e.

$$\beta = \beta_0 + \kappa X' \quad (23)$$

where κ is the bias gradient, and β_0 is the constant part of the bias error. The FS harmonic amplitudes and phases ($n \neq 0$) for the biased and unbiased cases are related as follows:

$$\begin{aligned} a_n &= \frac{2}{T'} \int_0^{T'} (1 + \kappa) X'(t) \cos(2\pi n f t) dt \\ &+ \frac{2}{T'} \int_0^{T'} \beta_0 \cos(2\pi n f t) dt \\ &= (1 + \kappa) \frac{2}{T'} \int_0^{T'} X'(t) \cos(2\pi n f t) dt + 0 = (1 + \kappa) a'_n \end{aligned} \quad (24)$$

$$b_n = (1 + \kappa) b'_n \quad (25)$$

$$X_n = \sqrt{a_n^2 + b_n^2} = (1 + \kappa) X'_n \quad (26)$$

$$\gamma_n = \tan^{-1} \left(\frac{(1 + \kappa) b'_n}{(1 + \kappa) a'_n} \right) = \tan^{-1} \left(\frac{b'_n}{a'_n} \right) = \gamma'_n \quad (27)$$

wherein a' , b' , X'_n and γ' are for the unbiased case. The bias errors for the FS harmonic amplitudes and phases can then be determined as

$$\beta_{X_n} = X_n - X'_n = \frac{\kappa}{1 + \kappa} X_n \quad (28)$$

$$\beta_{\gamma_n} = \gamma_n - \gamma'_n = 0 \quad (29)$$

The above deductions indicate that the bias error of the FS harmonic amplitude does not directly depend on the bias error, but on the bias gradient of the measured variable. Also, the bias error of the FS harmonic phase is independent of the bias error of the measured variable X . According to Eq. 28, the bias limits of the FS harmonic amplitudes can be determined as

$$B_{X_n} = \frac{\kappa^*}{1 + \kappa^*} X_n \quad \text{for } n \neq 0 \quad (30)$$

where κ^* is the limit (maximal magnitude) of the bias gradient, which can be calculated with the data-reduction equation and elementary bias limits. The bias limit of the zeroth FS harmonic amplitude is determined as

$$B_{X_0} = \frac{2}{T'} \int_0^{T'} B_X dt = 2 \overline{B_X} \quad (31)$$

According to Eq. 29 the bias limits of the FS harmonic phases equal zero, i.e. $B_{\gamma_n} = 0$. The bias limits of the adjusted phases ($B_{\Delta\gamma_n}$) are then determined with Eq. 11 and equations for determining the reference phase γ_I . For example, the bias limits of the adjusted harmonic phases for the forces and moment are determined with Eqs. 11 and 16 as

$$B_{\Delta\gamma_{CT,n}} = B_{\Delta\gamma_{CH,n}} = B_{\Delta\gamma_{CM,n}} = \theta_D B_D = 2\pi \frac{B_D}{\lambda} \quad (32)$$

The precision limit and the total uncertainty for the FS harmonics are determined with the same procedures as for the time histories.

3.2

Reconstructed time histories

The data reduction equation for a FS-reconstructed time history can be represented as

$$X_F(t) = X_F(X_0, X_1, X_2, \dots, X_N, \Delta\gamma_1, \Delta\gamma_2, \dots, \Delta\gamma_N, t) \quad (33)$$

where N is order of the FS. For the reconstructed time history, time t is a given value, so it has neither bias nor precision errors. According to the data reduction equation, the precision limit are determined with

$$P_{X_F} = \sqrt{(\theta_{X_0} P_{X_0})^2 + \sum_{n=1}^N (\theta_{X_n} P_{X_n})^2 + \sum_{n=1}^N (\theta_{\Delta\gamma_n} P_{\Delta\gamma_n})^2} \quad (34)$$

The sensitivity coefficients are

$$\theta_{X_0} = \frac{\partial X_F}{\partial X_0}, \theta_{X_n} = \frac{\partial X_F}{\partial X_n}, \theta_{\Delta\gamma_n} = \frac{\partial X_F}{\partial \Delta\gamma_n} \quad (35)$$

For reconstructed time histories, the bias limits can be estimated with the same procedure as for the raw time histories.

3.3

Summary of measurement uncertainties

Uncertainty assessments of the FS-reconstructed time histories are conducted for the forces and moment in the medium test case, i.e., $Fr = 0.28$, $\lambda = 0.3048$, and $Ak = 0.05$, and the results are given in Table 1. The precision limit (85–98%) is the main uncertainty source for the forces and moment coefficients, and the elementary precision limit for $\Delta\gamma$ is the main precision error source (61%–95%). C_H has a much larger precision error for determining $\Delta\gamma$ than C_T and C_M , so that its relative uncertainty (9.76%) is much higher than those of C_T (4.23%) and C_M (2.93%). Uncertainty assessment results of the FS harmonics for C_T , C_H , C_M are provided in Table 2 with relative contributions of bias and precision components and total uncertainties normalized either with the first harmonic amplitudes for the zeroth and first harmonic and 2π for the phase. Again, the main contribution to the uncertainty in the FS harmonics is the precision limits.

Uncertainty assessments are conducted for free-surface elevations in the medium- Fr (0.28), long- λ (4.572), and low- Ak (0.025) case. A summary of the uncertainty assessments for the farfield free-surface elevations is provided in Table 3 at $y = 0.082$ and $y = 0.232$ for the steady and unsteady case, respectively. For the unsteady case, precision limits are determined at six phases and averaged. For both the steady and unsteady cases, the values are spatially averaged in the region of $x = 0 \sim 1$ and also time averaged for the unsteady case. Table 3 shows that the bias and precision limits are nearly the same order for both the steady and unsteady case. In the steady case, the bias limit is larger than the precision limit, but switched for the unsteady case. For both the steady and unsteady cases, the main bias error source is from U_c . The uncertainty levels (1.5% and 3.3%) are reasonable.

Table 1. Uncertainty assessment for time histories

Term	CT	CH	CM
$P_{X,0}\theta_{X,0}$	5.46%	4.80%	20.2%
$P_{X,1}\theta_{X,1}$	15.7%	0.73%	18.9%
$P_{\Delta\gamma,1}\theta_{\Delta\gamma,1}$	78.8%	94.5%	60.9%
B_X	11.3%	14.1%	2.12%
P_X	88.7%	85.9%	97.9%
U_X	4.23% ^a	9.76% ^a	2.93% ^a

^aNormalized with X_1

Table 2. Uncertainty assessment for FS harmonics

Term	C_T	C_H	C_M
B_{X0}	38.2%	11.7%	2.21%
P_{X0}	61.8%	88.3%	97.8%
U_{X0}	1.08% ^a	12.3% ^a	2.80% ^a
B_{X1}	15.5%	18.19%	14.1%
P_{X1}	84.5%	81.9%	85.9%
U_{X1}	3.83% ^a	3.18% ^a	4.25% ^a
$B_{\Delta\gamma,1}$	0.45%	0.26%	0.70%
$P_{\Delta\gamma,1}$	99.5%	99.7%	99.3%
$U_{\Delta\gamma,1}$	3.62% ^b	6.24% ^b	2.32% ^b

^aNormalized with X_1

^bNormalized with 2π

Uncertainty assessment results for the nearfield free-surface elevation measurements are conducted at two points in the wavefield corresponding to high ($x = 1.075$, $y = 0$; HTR) and low ($x = 0.05$, $y = 0.07$; LTR) free-surface turbulence regions and summarized in Table 4. Note that for the unsteady cases, uncertainty assessments are completed for the FS-reconstructed time histories and the results are time averaged. For both steady and unsteady cases, precision limits are obtained with multiple tests ($N = 10$). Results for all cases demonstrate reasonable uncertainty levels of 1.1–4.2%. For the LTR, bias and precision limit contributions are equally weighted for the steady case, but for the unsteady case, the uncertainty value is dominated by a precision limit (84%). For the HTR and both steady and unsteady cases, the uncertainty values are dominated by precision limits, 75% and 87%, respectively.

4

Summary

Present investigations are aimed at procuring validation data for RANS CFD codes and explication of flow physics regarding DTMB model 5512 in regular head waves. In the first part of the paper, details of data reductions, measurement systems, and uncertainty assessment procedures are described. The results of uncertainty assessments demonstrate reasonable uncertainty levels of measurement data and indicate that the main uncertainty source for the forces, moment, and free-surface elevation measurements

Table 3. Uncertainty for farfield free-surface

Term	Steady, $y = 0.082$ Magnitude (%)	Unsteady, $y = 0.232$ Magnitude (%)
$B_{U_c}\theta_{U_c}$	3.0806×10^{-4} (79.3)	4.9762×10^{-4} (84.0)
$B_t\theta_t$	1.4364×10^{-7} (0.04)	2.3203×10^{-7} (0.04)
$B_D\theta_D$	2.2898×10^{-5} (5.89)	3.6988×10^{-5} (6.24)
$B_y\theta_y$	2.4636×10^{-5} (6.34)	2.5024×10^{-5} (4.22)
$B_z\theta_z$	3.2808×10^{-5} (8.44)	3.2808×10^{-5} (5.54)
B_ζ	3.12×10^{-4} (59.0)	5.01×10^{-4} (43.3)
P_ζ	2.17×10^{-4} (41.0)	6.55×10^{-4} (56.7)
U_ζ	3.80×10^{-4} (1.50) ^a	8.24×10^{-4} (3.25) ^a

^aNormalized with maximal $\zeta_{T,1}$

Table 4. Uncertainty for nearfield free-surface

Term	LTR: $x = 0.05$, $y = 0.07$ Magnitude (%)	HTR: $x = 1.075$, $y = 0$ Magnitude (%)
Steady ($Fr = 0.28$)		
B_ζ	3.2808×10^{-5} (52.6)	3.2808×10^{-5} (25.2)
P_ζ	2.9600×10^{-5} (47.4)	9.7200×10^{-5} (74.8)
U_ζ	4.4187×10^{-5} (1.10) ^a	1.0259×10^{-4} (1.90) ^a
Unsteady ($Fr = 0.28$, $\lambda = 4.572$ m, $Ak = 0.025$)		
$P_{\zeta,0}\theta_{\zeta,0}$	1.5754×10^{-4} (65.7)	1.5520×10^{-4} (40.1)
$P_{\zeta,1}\theta_{\zeta,1}$	5.2452×10^{-5} (21.9)	1.1498×10^{-4} (29.7)
$P_{\Delta\gamma,1}\theta_{\Delta\gamma,1}$	2.9945×10^{-5} (12.4)	1.1704×10^{-4} (30.2)
B_ζ	3.2808×10^{-5} (16.3)	3.2808×10^{-5} (12.7)
P_ζ	1.6872×10^{-4} (83.7)	2.2584×10^{-4} (87.3)
U_ζ	1.7188×10^{-4} (2.86) ^a	2.2821×10^{-4} (4.23) ^a

^aNormalized with local $\zeta_{T,1}$

is the precision error. The precision error can be reduced in the future by improving the stability of the measurement systems and by increasing the recording time for unsteady signals. For the farfield free-surface measurement, the bias limit is as significant as the precision limit and the main bias error results from the carriage speed. Therefore, the speed of the carriage should be controlled better for future unsteady tests. For the nearfield free-surface measurement and steady case, bias and precision limits are comparable, whereas for the unsteady cases precision limits are much larger than the bias limits. The measurement data and discussions on the flow physics are presented in the second part of the paper (Gui et al. 2001).

References

- Alessandrini B; Delhommeau G** (1999) A fully coupled Navier-Stokes solver for calculation of turbulent incompressible free surface flow past a ship hull. *Int J Numer Methods Fluids* 29: 125–142
- American Institute of Aeronautics & Astronautics (AIAA) (1999) Assessment of experimental uncertainty with application to wind tunnel testing. AIAA Standard AIAA S-017A-1999. American Institute of Aeronautics & Astronautics, Reston, Va.
- Arabshahi A; Beddhu M; Briley W** (1998) A Perspective on naval hydrodynamic flow simulations. In: 22nd ONR Symposium on Naval Hydro, 1998, Washington DC. pp 920–934
- Gui L; Longo J; Metcalf B; Shao J; Stern F** (2001) Forces, moment, and wave pattern for surface combatant in regular head waves. II. Measurement results and discussions. *Exp Fluids* (in press)
- ITTC (1999) Report of the Resistance and Flow Committee. In: 22nd International Towing-Tank Conference, 1999, Seoul, Korea/Beijing, China. pp 173–246
- Journee JMJ** (1992) Experiments and calculations on four Wighey hullforms. Delft, Report No. 909. Ship Hydromechanics Lab, Delft University of Technology, Delft, The Netherlands
- Kanai M** (1985) Wave analysis by grid projection method. *J Soc Nav Archit Jpn* 193: 127–135
- Landrini M; Grytoyr G; Faltinsen OM** (1999) A B-spline-based BEM for unsteady free-surface flows. *J Ship Res* 43: 13–24
- Longo J; Rhee SH; Kuhl D; Metcalf B; Rose R; Stern F** (1998) IIHR towing-tank wavemaker. In: 25th ATTC, 1998, Iowa City, Iowa, pp 6.32–6.52
- Nishio S; Nakao S; Okuno T** (1998) Image measurement of the wave height distributions around a ship hull in regular wave. *J Soc Nav Archit Jpn* 184: 95–102
- Ohkusu M** (1990) Added resistance in waves in the light of unsteady wave pattern analysis. In: 13th ONR Symposium, 1990, Japan, pp 413–426
- Rhee SH; Stern F** (1998) Unsteady RANS method for surface ship boundary layer and wake and wave field. In: 3rd Osaka Colloquium on Advanced CFD Applications to Ship Flow and Hull Form Design, 25–27 May 1998, Osaka, Japan, pp 67–84
- Stern F; Longo J; Maksoud M; Suzuki T** (1998) Evaluation of surface-ship resistance and propulsion model-scale database for CFD validation. In: 1st Symposium on Marine Applications of Computational Fluid Dynamics, 1998, McLean, Va, pp 129–156
- Wilson R; Paterson E; Stern F** (1998) Unsteady RANS CFD method for naval combatant in waves. In: 22nd ONR Symposium on Naval Hydro, 1998, Washington DC, pp 532–549